



The Effect of Contact Resistance on Short Wavelength Infrared Focal Plane Array Noise

E. C. Piquette¹

Received: 29 January 2024 / Accepted: 26 June 2024 / Published online: 10 July 2024
© The Minerals, Metals & Materials Society 2024

Abstract

Contact resistance can play a significant role in the noise performance of short wavelength infrared (SWIR) focal plane detector arrays (FPAs), particularly during cryogenic operation at low signal backgrounds. For astronomy FPAs, a source follower input cell ROIC is typically used in combination with correlated double sampling (CDS) or a form of up-the-ramp (SUTR) multi-sampling. In this paper, a pixel equivalent circuit model is presented and analyzed by standard techniques. The noise power density spectrum is analyzed for CDS and multi-sampled acquisitions, and it is found that there are three distinct ranges of contact resistance that govern excess noise behavior: the low-noise ROIC-limited range, the intermediate kTC-limited range, and the RC-bandwidth limited case. The model analyses are used to explain FPA data from Teledyne H2RG and H4RG SWIR FPAs. We have found that sampling sequence in combination with contact resistance can influence the total integrated noise, and can explain a FPA failure mode where anomalously low CDS and anomalously high SUTR noise exist in the same region.

Keywords HgCdTe · contact resistance · H2RG · H4RG · infrared · astronomy · SWIR

Introduction

Short wavelength infrared (SWIR) focal plane arrays (FPAs) have proven to be productive tools for infrared astronomy in both ground and space observatories. A significant metric in the utility of SWIR sensors, for both science throughput and scope, is the signal-to-noise ratio (SNR) of the captured images. The higher the sensitivity and the lower the noise, the fainter the objects that can be seen, with the least amount of exposure time.

The signal is generally limited by the telescope aperture and optics, and by the quantum efficiency (QE) of the detectors, where typical HgCdTe-based detectors achieve QE values greater than 90%, approaching physical limits without gain. As large-format SWIR avalanche photodiode arrays are currently unavailable with large gain and low noise factor, improving SNR by QE improvement has plateaued.

The other means of improving SNR is by reduction of image noise. For brighter objects, the noise is typically limited by signal shot noise, equal to the square root of the number of integrated charges (in units of electrons), and SNR is usually adequate. For very faint signals, however, which are generally of highest interest, noise is more often limited by detector dark current noise or FPA read noise. Dark current may be mitigated through cryogenic cooling, leaving read noise as the limiting performance driver. While multi-sampling schemes such as sample up the ramp (SUTR) or Fowler sampling^{1,2} can improve noise through statistical averaging, some sources of excess noise in the detector, such as 1/f noise, can limit the sampling noise reduction.

The FPAs considered here are hybrids of a detector array indium bump bonded to a read-out integrated circuit (ROIC) used to multiplex the detector pixel outputs. Both hybrid components can contribute to the FPA noise. For the detector pixel array, there are several mechanisms that can contribute, including excess noise from charge trapping effects at material defects, contact thermal noise, dark current shot noise, and 1/f noise from surface recombination velocity modulation. From the ROIC, we have contributions from CMOS transistor noise, coupled power supply noise, jitter

✉ E. C. Piquette
eric.piquette@teledyne.com

¹ Teledyne Imaging Sensors, 5212 Verdugo Way, Camarillo, CA 93012, USA

noise, fixed pattern noise due to silicon chip foundry non-uniformity, and others.

In this work, we limit the analysis to the excess noise contribution from the contact resistance thermal (Johnson) noise.³ We neglect series resistance arising from the substrate sheet resistance (DSUB), which is typically orders of magnitude lower than the pixel contact resistance. This is most often because of the high mobility of the absorber layer charge carriers and the presence of numerous DSUB contacts. The pixel contact resistance tends to be dominant in *p-on-n* HgCdTe FPAs (considered below) due to use of a wider band-gap *p*-type cap material, which has traditionally offered a challenge in formation of ohmic contacts, operating cold.

We describe an equivalent circuit for the pixel, from which we can estimate parasitic capacitance and voltage division effects between the contact noise source and the integration node, obtaining the commonly used “input referred” noise values. The equivalent circuit analysis results in gain and noise bandwidth effects. We then compare the model predicted noise versus measured FPA noise for correlated double sample (CDS) and SUTR sampling cadences.

Noise Model and Analysis

The noise analysis is relevant to photodiode detectors hybridized to source follower ROIC. Figure 1a shows the typical arrangement, as, for example, in the Teledyne H2RG FPA which uses HgCdTe *p-on-n* photodiode detectors. The detector array is typically multiplexed by row and column of the array, and a sequence of frames is acquired. For each frame, the photodiodes are reset to a negative bias relative to the detector substrate (DSUB), then the reset switch is opened to leave the detector node bias (the source follower gate) to slew towards DSUB as currents (dark and signal) flow

through the junction and the photodiodes de-bias (Fig. 1b). The pixel voltage is read after t_{int} (the integration time). The amount of charge integrated on the detector can then be determined by converting the measured node voltage into charge by the conversion gain capacitance ($Q = VC$). The per-pixel detector noise can be estimated by calculating the standard deviation of the measured signals on each frame.

To calculate the noise for this situation, we constructed an equivalent circuit for the physical photodetector and propagated the contact resistance noise source element to the noise seen on the ROIC pixel node. We then considered the impact on integrated input referred noise for different sampling schemes, such as single-read (SR), CDS, and SUTR.

Figure 2 shows a cross-section of the traditional planar HgCdTe photodiode detector, also referred to as the double-layer planar heterojunction detector.⁴ The figure is not to scale, but indicates the relevant main and parasitic capacitances of the detector, along with the resistance of the metal contact. The main capacitance elements are: C_D , the main diode capacitance across the depletion region of the *pn* junction; C_{PM} , the capacitance between node interconnect metal and the DSUB; C_C , the capacitance between the metal contact

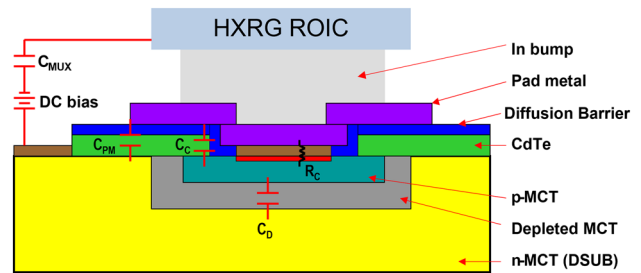


Fig. 2 Cross-section of the planar HgCdTe photodiode, as hybridized to the ROIC input cell via indium interconnect, with equivalent circuit elements.

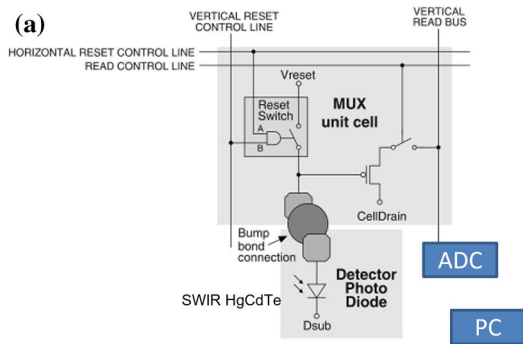
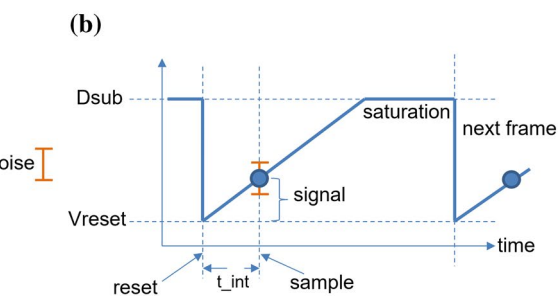


Fig. 1 Left Schematic of the HXRG ROIC unit cell, as hybridized to the HgCdTe photodiode detector. Right The pixel node voltage as signal is accumulated in the pixel, which de-biases the photodiode and the source follower gate voltage swings from V_RESET to DSUB.



Noise is measured by acquiring a number of repeated frames, and calculating the standard deviation of the measured voltage values for each pixel.

and the *p*-HgCdTe (across the contact); and C_{MUX} , the ROIC total node capacitance, which is mainly the source follower transistor gate-source and gate-emitter capacitance. Also note that assuming the contact is making a Schottky contact to the *p*-HgCdTe, there will be a thin depletion region adjacent to the contact metal, which will add significant capacitance to C_C .

Figure 3 shows the extracted equivalent circuit from the detector cross-section of Fig. 2. We have manipulated the circuit to isolate the noise generating element, R_C , and its simplified load, C_{BW} , which determines the RC circuit low-pass cutoff and bandwidth. Thus, for SRs, and neglecting other noise sources including reset kTC noise, the contact integrated noise is:

$$v_{n1} = \sqrt{4kTR_C\Delta F}[\text{Volts}], \text{ where } \Delta F = \frac{1}{4R_C C_{BW}}, \tag{1}$$

$$\text{and } C_{BW} = C_C + \frac{C_M C_D}{C_M + C_D}$$

where $C_M = C_{MUX} + C_{PM}$. However, this is the noise across the contact itself, whereas the relevant measured noise is the variation of the node voltage with respect to the ground (DSUB). The detector noise is related to the contact noise by the voltage divider:

$$v_n = v_{n1} \frac{C_D}{C_D + C_M} [\text{Volts}] \tag{2}$$

In units of electrons, and substituting for Δf , the integrated noise is:

$$q_n = \frac{C_d}{q} \sqrt{\frac{kT}{C_{BW}}} [\text{electrons}] \tag{3}$$

The noise spectral density is of the form common for Johnson noise in RC circuits and can be expressed in units of volts squared per hertz as:

$$v_n^2(f) = \left(\frac{C_D}{C_D + C_M} \right)^2 \frac{4kTR_c}{1 + (2\pi f R_c C_{BW})^2} \tag{4}$$

This is the Lorentzian⁵ noise form with self-limiting (RC) bandwidth. In the cases where the noise is limited by a video filter, for purposes of white noise reduction, or by multi-sampling, the noise spectral density is modified by additional terms corresponding to these filters. A typical analog video filter can be modeled as a multi-pole low pass filter (of order *n*, where f_v is the filter frequency corner) of the form:

$$h_{\text{video}}(f) = \frac{1}{1 + (f/f_v)^{2n}} \tag{5}$$

Figure 4 shows example noise power spectral density curves for three different contact resistance values: 10 kOhms, 10 MOhms and 10 GOhms, as well as the low pass video filter frequency curve for the example of $f_v = 200$ kHz, $n = 2$. We see that for low values of contact resistance (10 kOhms), the noise spectral density in the “white” region, below RC corner frequency, is low, near $1\text{E}-16$ V²/Hz, and the RC bandwidth is near 1 GHz. For high contact resistance, of 10 MOhms, the low-frequency white noise density increases to $\sim 1\text{E}-13$ V²/Hz and the bandwidth reduces to 1 MHz. And for very high contact resistance, for those cases where the contact is severely impaired (10 GOhms), the noise density increases

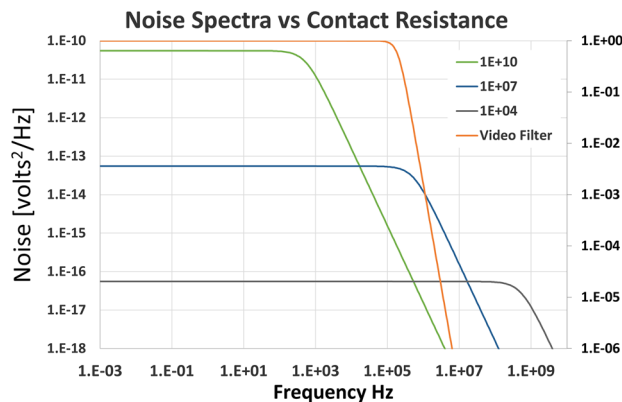


Fig. 4 Noise spectral density, in units of volts-squared per Hz, for three example contact resistances and an example video filter.

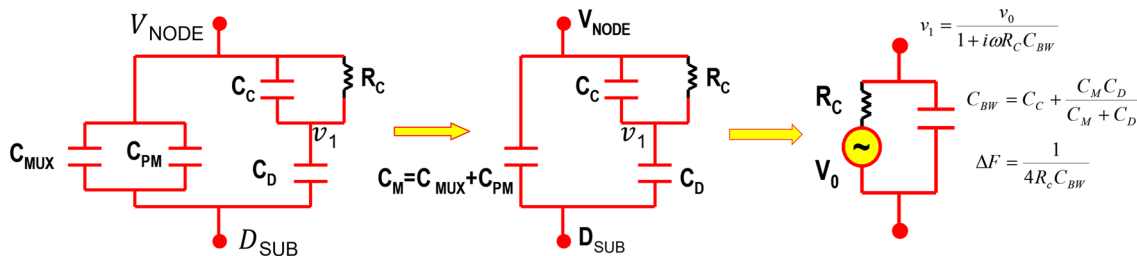


Fig. 3 Simplification of the detector-input cell equivalent circuit, with load as seen by the contact resistance.

to $\sim 1\text{E}-10 \text{ V}^2/\text{Hz}$, and the bandwidth is only 1 kHz. For these cases, and for the video filter example shown, the low contact resistance noise will be considerably reduced by the video filter, while the higher resistance values will be bandwidth self-limited, and their integrated noise will be given by Eqs. 2 and 3. It is therefore optimal, and, for lowest noise, the contact resistance and video filter corner frequency will both be minimized to achieve the lowest read noise. When this is achieved, read noise is, in practice, limited by ROIC downstream noise. The video filtered noise is given by:

$$q_n = \frac{C_d}{q} \sqrt{4R_c kT \Delta f_{\text{video}}} [e^-]; q_n^2 = \int \left(\frac{C_D}{q} \right)^2 \left(\frac{4kTR_c}{1 + (2\pi f R_c C_{BW})^2} \right) \left(\frac{1}{1 + (f/f_v)^{2n}} \right) df \quad (6)$$

The above analysis is the case for single sample reads of the pixel node voltage, neglecting reset kTC noise and multi-sampling. One common sampling cadence used with source follower ROICs, the main purpose of which is the elimination of reset (pedestal) noise, is CDS. In this technique, the sensor is reset, then two non-destructive frames are sampled. The first frame is subtracted from the second on a per-pixel basis. This differencing has the effect of eliminating ROIC offset non-uniformity and reset noise, with the penalty of an increase of doubling of the noise variance (root two increase in noise electrons). The CDS sampling is straightforward in its impact for the case of white noise, but, for the filtered noise spectra considered above, the interaction is slightly more complicated. The effective frequency filtering effect of the CDS sampling is the Fourier transform of the difference of two

time-separated delta functions, which goes as sin squared (t_{int} is the integration time):

$$h_{\text{CDS}}(f) = 4\sin^2(\pi f t_{\text{int}}) \quad (7)$$

Note that, in the low-frequency limit, the CDS filter kernel goes as approximately f -squared (a high pass filter), and for high frequencies is rapidly oscillating with an average value of 2. It is this factor of two in the high-frequency band that corresponds with the doubling of samples and noise variance.

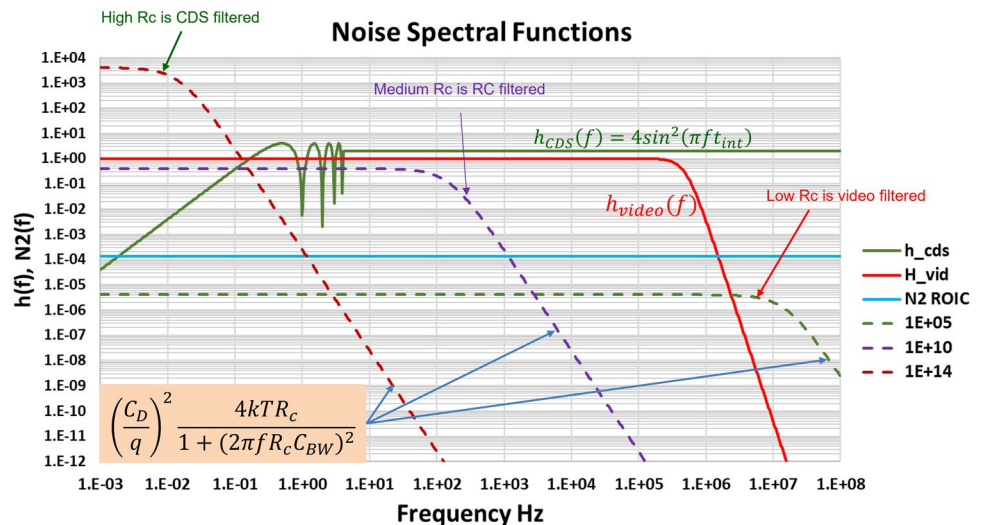
The combined noise equation, including analog filtering and CDS sampling, is given by:

$$q_n^2_{\text{CDS}} = \int \left(\frac{C_D}{q} \right)^2 4\sin^2(\pi f t_{\text{int}}) \left(\frac{4kTR_c}{1 + (2\pi f R_c C_{BW})^2} \right) \left(\frac{1}{1 + (f/f_v)^{2n}} \right) df \quad (8)$$

The first product term inside the integral is the combined transimpedance gain and voltage division gain, the second is the CDS filter term, the third is the contact resistance Johnson noise Lorentzian, and the fourth is the video low pass filter. The integral runs from zero Hz to infinity.

Figure 5 shows the noise spectral components for CDS sampling for three different contact resistance values (1E5, 1E10, and 1E14 Ohms). For the low contact resistance, we see that, as in the single sampling case, the video filter determines the bandwidth and the high-frequency filter of the CDS sampling is insignificant. We see that the excess noise from contact resistance remains below the ROIC noise at all frequencies, so we expect that the total read noise for contact resistances near 1E5 Ohms should be flat versus resistance, and dominated by the ROIC.

Fig. 5 Noise spectral density, including the spectral equivalent filter for CDS sampling (1 s integration time).



Considering Fig. 5 for the 1E10 Ohms contact resistance, again the CDS high pass filter is not significantly reducing the noise bandwidth, which is below the video filter frequency and dominated by the RC time constant of the pixel, with noise given by Eq. 3, and again independent of resistance. For very high contact resistance values ($\sim 1\text{E}14$ Ohms), we see that the RC filter frequency is now very low and comparable to the high pass CDS cut-on frequency. This has the effect that the CDS sampling significantly reduces the read noise, as the pixel does not have the slow rate to change much between CDS samples. The predicted noise spectral density of Figs. 4 and 5 can be compared to the measured spectra of Smith et al.⁶, where we see good agreement in the presence of a low-pass Lorentzian knee near 100–1000 Hz for 1.7 μm cutoff detectors.

Figure 6 shows the model-predicted read noise versus contact resistance, compared with measured median values from H2RG astronomy FPAs. Good, low contact resistance arrays are included as well as data from FPAs with poor contacts. The contact resistance measurements for the FPAs were taken using special contact structures on evaluation chips, which were adjacent on the process wafer to the FPA detector die. Separate n , p , and sheet resistance contact structures allowed us to isolate the dominant series resistance in the detector array with the pixel p -contacts. We see that the model predicts the overall qualitative behavior very well, but there is some scatter in the measured data points. This variability may be attributed to differences in HgCdTe doping levels and pixel layer thicknesses, which slightly change the parasitic capacitance values in the extracted elements of Fig. 2. Parameter values used for the model are: $T = 78$ K, $C_D = 17.4$ fF, $C_{\text{BW}} = 92.7$ fF, $C_M = 16$ fF, and $f_v = 5\text{E}5$ Hz.

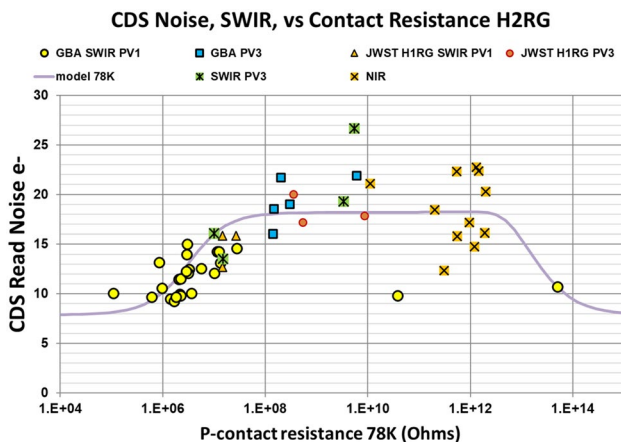


Fig. 6 The predicted integrated noise, in electrons, as a function of contact resistance. Also shown are measured FPA median CDS noise values for short cutoff wavelength HXRg FPAs.

We observe that the range of measured contact resistances cover several orders of magnitude and demonstrate the relative difficulty of obtaining ohmic contacts to p -type SWIR HgCdTe at cryogenic temperatures. Resistive and Schottky contacts can occur from a number of causes, including (1) metal interaction with the HgCdTe, forming Schottky barriers, (2) HgCdTe native oxide, (3) type conversion of the p -type material near the contact from the gettering of impurities, mercury interstitials, or local damage, (4) poor indium bump interconnect formation, or (5) unintentional contamination of the contact stack between the HgCdTe and the ROIC input cell, such as from lithography organics. Attribution of the cause of higher resistance must be on a case-by-case basis and is not addressed here.

The procedure for modeling the noise spectral density for other sampling cadences uses the same approach, taking the Fourier transform of the time domain sampling. Here, we can briefly consider one popular multi-sampling cadence, which is SUTR, for which a number of sequential frames are non-destructively read, and the per-pixel signal is derived by fitting linear regression slope and residual to the measured sequence of frame values. When SUTR uses enough samples, the effective filtering becomes similar to that of an integrator transform, which has frequency domain shape of the sinc function:⁷

$$h_{\text{SUTR}}(f) \sim \frac{\sin^2(\pi f t_{\text{int}})}{(\pi f)^2} \quad (9)$$

Figure 7 (left) shows the predicted noise spectral density curves for the SUTR case. The SUTR acts as a low-pass filter, compounding the effect of low-frequency noise for the case of high contact resistances. Figure 7 (right) shows the predicted integrated noise values versus contact resistance for CDS and SUTR sampling conditions. We see that, for high contact resistances, the predicted CDS noise falls below 10e^- , while the SUTR noise increases rapidly for contact resistances above $1\text{E}9$ Ohm.

The difference in noise behavior for the CDS and SUTR sampling is useful in explaining observations made in data from several FPAs made for the Nancy Grace Roman Space Telescope.⁸ These FPAs use the Teledyne H4RG-10 ROIC, are of format $4\text{K} \times 4\text{K}$, with $10\text{-}\mu\text{m}$ pixel pitch and $2.5\text{-}\mu\text{m}$ cutoff wavelength. Noise was measured at 95 K for both CDS and SUTR multi-sampling modes. Figure 8 shows example maps where a rare failure mode was seen in the flight production FPAs, in which large regions of pixels showed anomalously low CDS noise, concurrently with anomalously high SUTR noise in the same regions. While the root cause for these failed FPAs was not explicitly determined, the modeling above suggests that a cause such as organic contact contamination or poor indium interconnection, resulting

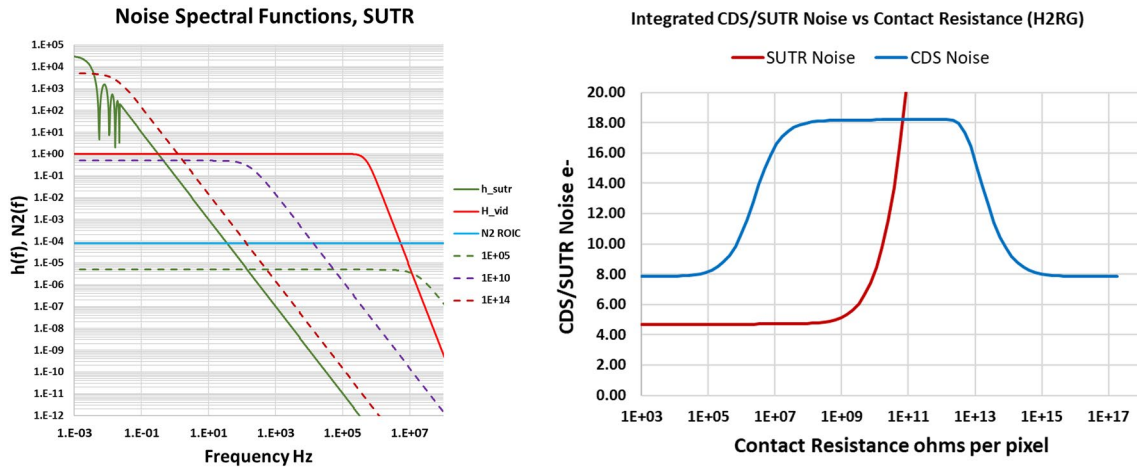
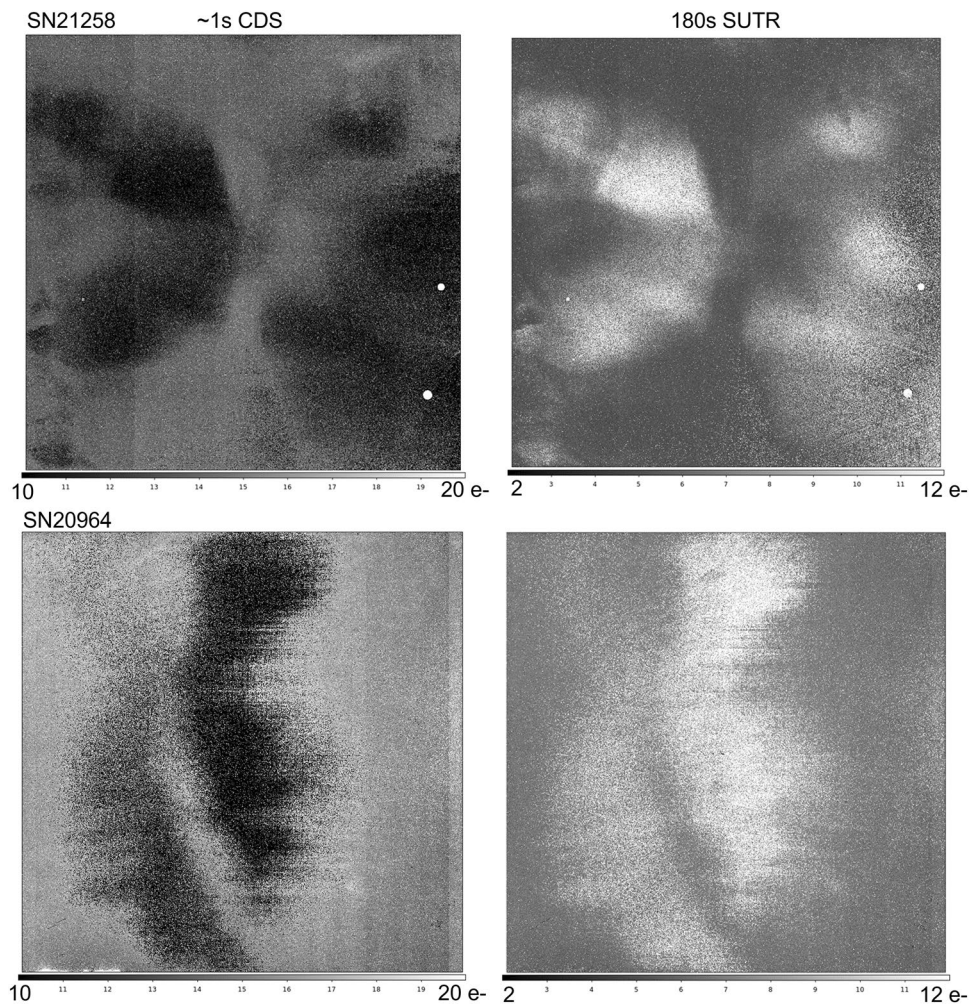


Fig. 7 *Left* Noise spectral density model including the spectrum for SUTR sampling. *Right* Total integrated noise in electrons for CDS and SUTR sampling cadences.

Fig. 8 Noise maps for anomalous H4RG-10 2.5- μ m cutoff FPAs made for the Roman Space Telescope. We see map features where CDS noise is anomalously low while SUTR noise is anomalously high. This behavior can be explained in the case of very high series resistances.



in very high series resistance, would be consistent with the data.

Finally, care should be taken in analysis of multi-sampling noise, for the cases where the noise spectral density

is not white over the multi-sampling effective frequency range. In general, analysis such as that by Rauscher¹ will be modified by the presence of excess contact resistance, since the contact noise spectral density can be strongly changing with frequency. In these cases, the full noise integral which includes the sampling cadence filter frequency response (Fourier transform of time sampling), is required rather than statistical sampling regressions which may assume white CDS noise.

Conclusions

Contact resistance can add excess noise to infrared FPAs, particularly in configurations which use source follower input cell ROICS, such as the Teledyne HXRG family. The behavior of CDS noise is predicted to fall into three regions: the low-resistance region, where the noise is dominated by the ROIC, the intermediate region, where noise is dominated by contact kTC noise (independent of R), and the high-resistance range, where the CDS sampling acts as a high pass filter, reducing the noise again. Other sampling cadences such as SUTR are expected to increase in noise monotonically with contact resistance. The different behavior between CDS and SUTR sampling can give rise to cases where CDS noise is anomalously low and SUTR noise is anomalously high. Example FPA noise data have been shown confirming the model predicted noise behavior, with some amount of variability. This noise analysis approach, using a detector equivalent circuit combined with that of the ROIC input cell, is generally applicable to FPAs of any sensing material, cutoff wavelength, and operating temperature, which use a source follower input cell. While results were shown for SWIR HgCdTe at 95 K, similar results are obtained for 1.7- μm detectors (which tend to be even more limited by contact resistance), while longer wavelength detectors, where contacts are made to narrower band-gap material, tend to allow generally lower contact resistance, and therefore tend to remain in the ROIC dominant regime.

Acknowledgment The authors would like to thank and acknowledge the Nancy Grace Roman Space Telescope Detectors Team at NASA Goddard, including John Gyax, Analia Cillis, Roger Foltz, and Mario Cabrera, for use of FPA test data shown in Figure 8.

Conflict of Interest The authors declare that they have no conflict of interest.

References

1. B.J. Rauscher, O. Fox, P. Ferruit, R.J. Hill, A. Waczynski, Y. Wen, W. Xia-Serafino, B. Mott, D. Alexander, C.K. Brambora, R. Derro, C. Engler, M.B. Garrison, T. Johnson, S.S. Manthripragada, J.M. Marsh, C. Marshall, R.J. Martineau, K.B. Shakoorzadeh, and P. Strada, Detectors for the *James Webb Space* telescope near-infrared spectrograph. I. Readout mode, noise model, and calibration considerations. *Publ. Astron. Soc. Pac.* 119(857), 768 (2007). <https://doi.org/10.1086/520887>.
2. B.J. Rauscher, Erratum. *Publ. Astron. Soc. Pac.* 122, 1254 (2010).
3. https://en.wikipedia.org/wiki/Johnson-Nyquist_noise
4. A. D'Souza, J. Bajaj, R.E. DeWames, D.D. Edwall, P.S. Wijewarnasuriya, and N. Nayar, MWIR DLPH HgCdTe photodiode performance dependence on substrate material. *J. Electron. Mater.* 27, 727 (1998).
5. http://www.scholarpedia.org/article/1/f_noise
6. R. Smith, C. Bebek, M. Bonati, M.G. Brown, D. Cole, G. Rahmer, M. Schubnell, S. Seshadri, and G. Tarle, Noise and zero point drift in 1.7 μm cutoff detectors for SNAP. In: Proc. SPIE 6276, High Energy, Optical, and Infrared Detectors for Astronomy II, 62760R (2006) <https://doi.org/10.1117/12.672616>.
7. https://en.wikipedia.org/wiki/Sinc_function
8. <https://roman.gsfc.nasa.gov/>

Publisher's Note Springer Nature remains neutral with regard to jurisdictional claims in published maps and institutional affiliations.

Springer Nature or its licensor (e.g. a society or other partner) holds exclusive rights to this article under a publishing agreement with the author(s) or other rightsholder(s); author self-archiving of the accepted manuscript version of this article is solely governed by the terms of such publishing agreement and applicable law.